Steel and Composite Structures, *Vol. 26, No. 4 (2018) 439-452*
DOI: https://doi.org/10.12989/scs.2018.26.4.439

Ultra-low cycle fatigue tests of Class 1 H-shaped steel beams under cyclic pure bending

Xianzhong Zhao [*1], Yafeng Tian [1a], Liang-Jiu Jia [2b] and Tao Zhang [1a]

[1] *Deparment of Structural Engineering, Tongji University, Shanghai, 200092, China*
[2] *Research Institute of Structural Engineering and Disaster Reduction, Tongji University, Shanghai, 200092, China*

(*Received September 9, 2017, Revised December 4, 2017, Accepted December 5, 2017*)

Abstract. This paper presents experimental and numerical study on buckling behaviors and hysteretic performance of Class 1 H-shaped steel beam subjected to cyclic pure bending within the scope of ultra-low cycle fatigue (ULCF). A loading device was designed to achieve the pure bending loading condition and 4 H-shaped specimens with a small width-to-thickness ratio were tested under 4 different loading histories. The emphasis of this work is on the impacts induced by local buckling and subsequent ductile fracture. The experimental and numerical results indicate that the specimen failure is mainly induced by elasto-plastic local buckling, and is closely correlated with the plastic straining history. Compared with monotonic loading, the elasto-plastic local buckling can occur at a much smaller displacement amplitude due to a number of preceding plastic reversals with relative small strain amplitudes, which is mainly correlated with decreasing tangent modulus of the material under cyclic straining. Ductile fracture is found to be a secondary factor leading to deterioration of the load-carrying capacity. In addition, a new ULCF life evaluation method is proposed for the specimens using the concept of energy decomposition, where the cumulative plastic energy is classified into two categories as isotropic hardening and kinematic hardening correlated. A linear correlation between the two energies is found and formulated, which compares well with the experimental results.

Keywords: ultra-low cycle fatigue; local buckling; ductile fracture; pure bending; H-shaped beam

1. Introduction

H-shaped steel beams have been widely employed in steel structures for their good flexural behaviors and convenient connection details. Currently, 4 classes of cross sections, i.e., plastic section, compact section, semi-compact section and slender section are defined in some design specifications (Davies and Brown 1996) for H-shaped steel beams according to their susceptibility to local buckling (Shokouhian and Shi 2014). For Class 1 cross section (plastic section), local buckling can hardly happen during the elastic stage under monotonic loading and full plastic moment resistance can be developed with sufficient rotation capacity (Cheng *et al*. 2013), which is favorable to seismic design.

In the past few decades, an extensive amount of research has been conducted to investigate H-shaped steel beams. Hall (1954), Ko *et al*. (2000) and Yasuhiro *et al*. (2000) investigated deformation characteristics of H-shaped beams subjected to shear forces. Gioncu and Petcu (1997a, b), Hasegawa and Ikarashi (2014) and Nakashima (1994) conducted experimental investigation on rotational capacity and strength of H-shaped beams under combined compression and bending. Anastasiadis *et al*. (2012) and Gioncu *et al*. (2012) developed a prediction method for rotational capacity and ductility of members under cyclic loading. Elkady and Lignos (2015), Newell and Uang (2008), Lee and Lee (1994) studied ductility and strength of H-shaped beams and columns under cyclic loading. In addition, local buckling of Class 1 H-shaped link beams under cyclic shear and bending was investigated (e.g., Kasai and Popov 1986a, b, Richards and Uang 2005), where the final limiting state was local buckling of the webs. However, the case under cyclic pure bending has seldom been investigated, where the limiting state may be different from the ones under cyclic combined shear and bending.

Recognizing the fact that local buckling can reduce strength and ductility of a structural member and even lead to structural collapse, research on local buckling has been intensively conducted (Akrami and Erfani 2015). Shinji (2003), Keisuke *et al*. (2006), Lin *et al*. (2002, 2003), Noritada *et al*. (2002) and Dawei *et al*. (2003) investigated inelastic lateral torsional buckling behaviors of H-shaped beams under axial force or bending. There are also many studies (Dawei *et al*. 2003, Niu *et al*. 2014, Kubiak *et al*. 2016, Shokouhian *et al*. 2016) on the coupling effect of local and global buckling of beams with different materials or cross sections. Besides, there are a number of studies on ultra-low cycle fatigue (ULCF) behaviors of metal structures, e.g., (Ge *et al*. 2014, Jia *et al*. 2014, 2016, Chen *et al*. 2017, Liu *et al*. 2017, Xiang *et al*. 2017a, b). However, research on local buckling of Class 1 H-shaped section under cyclic pure bending is limited especially under ULCF loading, and the coupling effect of local

∗Corresponding author, Professor,
E-mail: x.zhao@tongji.edu.cn
[a] Ph.D. Student, E-mail: 82tyf@tongji.edu.cn
[b] Associate Professor, E-mail: lj_jia@tongji.edu.cn

http://www.techno-press.org/?journal=scs&subpage=6
ISSN: 1229-9367 (Print), 1598-6233 (Online)

buckling and fracture has seldom been investigated.

For Class 1 sections under ULCF loading with large plastic strain amplitudes, tangent stiffness of a specimen decreases remarkably after plastic strain reversals. Different loading histories can lead to distinguished local buckling behaviors of steel beams, which makes the mechanism of plastic buckling much more complicated than that under monotonic loading. In addition, H-shaped beams can still sustain a substantial amount of load-carrying capacity even after local buckling, and fracture may accelerate strength deterioration of the members.

The objective of the present work is to investigate interaction between local buckling and fracture of Class 1 H-shaped steel beams under cyclic pure bending in the ULCF range. In this paper, the impacts of such interaction on hysteretic characteristics including strength, stiffness, ductility and energy dissipation capacity of specimens under cyclic pure bending were emphatically studied. In addition, a finite element model was established to investigate the local stress-strain states and corresponding effect on local buckling of the H-shaped steel beams. Finally, a method to evaluate the ULCF life of the Class 1 H-shaped beams was proposed using a concept of energy decomposition, where the cumulative plastic energy was classified into isotropic hardening and kinematic hardening correlated energies.

2. Experimental facilities and arrangements

2.1 Design of specimens

The 4 H-shaped steel beams made of low alloy structural steel Q345B, with a nominal yield strength of 345 N/mm^2 were designed and manufactured in this study. The nominal length of each specimen was 1200 mm and all the specimens had the same section dimension of 270 mm × 200 mm × 6 mm × 16 mm (height × width × web thickness × flange thickness). The geometric dimensions are shown in Fig. 1 and the measured mechanical properties of the steel plates is shown in Table 1. The flanges and webs were butt welded and the weld toes were slightly polished according to common engineering practice. Two end plates were welded to the 2 ends of each specimen to connect with the loading beams illustrated in Fig. 2. Four stiffeners welded at the beam flange-to-end plate joint were designed, and also 4 stiffeners at the beam web-to-end plate joint. The length of the stiffeners at the web was designed to be longer than that at the flanges. This treatment is to avoid premature failure at the beam-to-end plate joints within the pure bending segment.

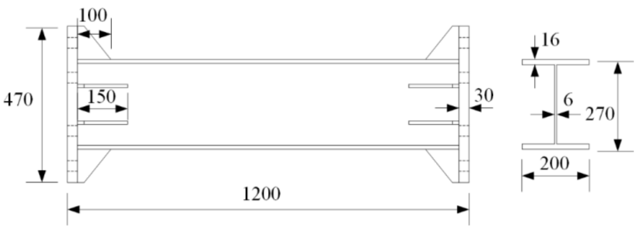

Fig. 1 Cross section of specimens

The flanges and webs are categorized into 4 classes based on the width-to-thickness ratio according to EC3 and the limiting values are listed in Table 2. In this study, both the webs and flanges of the specimens were designed as Class 1 and the detailed geometric parameters of the tested specimens are shown in the table.

2.2 Test setup

A testing device to achieve pure bending was designed and built to conduct the cyclic loading experiments in this study. The main components of the test setup are shown in Fig. 2. The device has 3 major parts: 2 loading beams, 2 identical actuators and 2 support columns. The actuators have a load capacity of ±2000 kN and the 2 loading beams are employed to transfer the loads from the actuators to the specimen. For the loading beams, one end was bolted to the tested specimen through rigid end plate connections and the other end was pin connected to the actuator. For the 2 support columns, both of the bottom ends were fixed to the ground through high-strength anchors, while one of the top end was pin connected to the loading beam and the other one was pin connected to a sliding connection shown in Fig. 2. The sliding connection consisted of a movable part and a fixed part with a sliding rail, where the frictional coefficient of the sliding rail is small to release axial deformation of the specimen due to the bending deformation, especially for the ULCF loading histories with large deformation. The sliding plate had a sliding displacement capacity of ±175 mm,

Table 1 Measured mechanical properties of steel

Nominal thickness (mm)	Actual thickness (mm)	Yield strength (MPa)	Tensile strength (MPa)	Strain at peak load	Elongation (%)
16	16.1	377	526	0.176	35.2
6	5.7	428	594	0.179	25.2

Table 2 Measured geometric parameters

$h \times b \times t_w \times t_f$	$c_w/t_w \leq X_w$	Web class	$c_f/t_f \leq X_f$	Flange class
270×200×6×16	39.7 ≤ 59.4	1	6.1 ≤ 7.4	1

*Notes: c_w: net height of web; c_f: net cantilevered width of flange; t_w: thickness of web; t_f: thickness of flange; X_w: critical ratio for web; X_f: critical ratio for flange (Eurocode 3 2005)

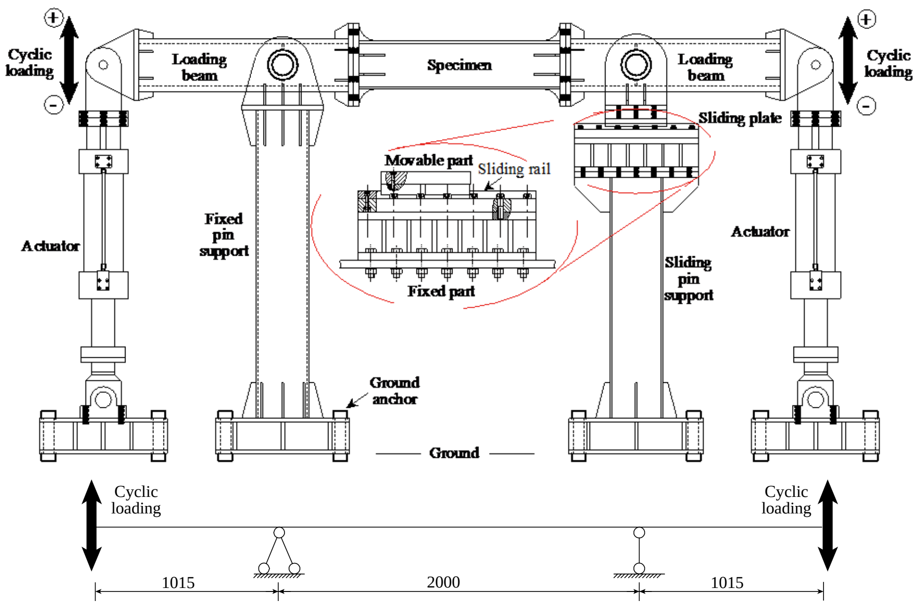

Fig. 2 Test setup

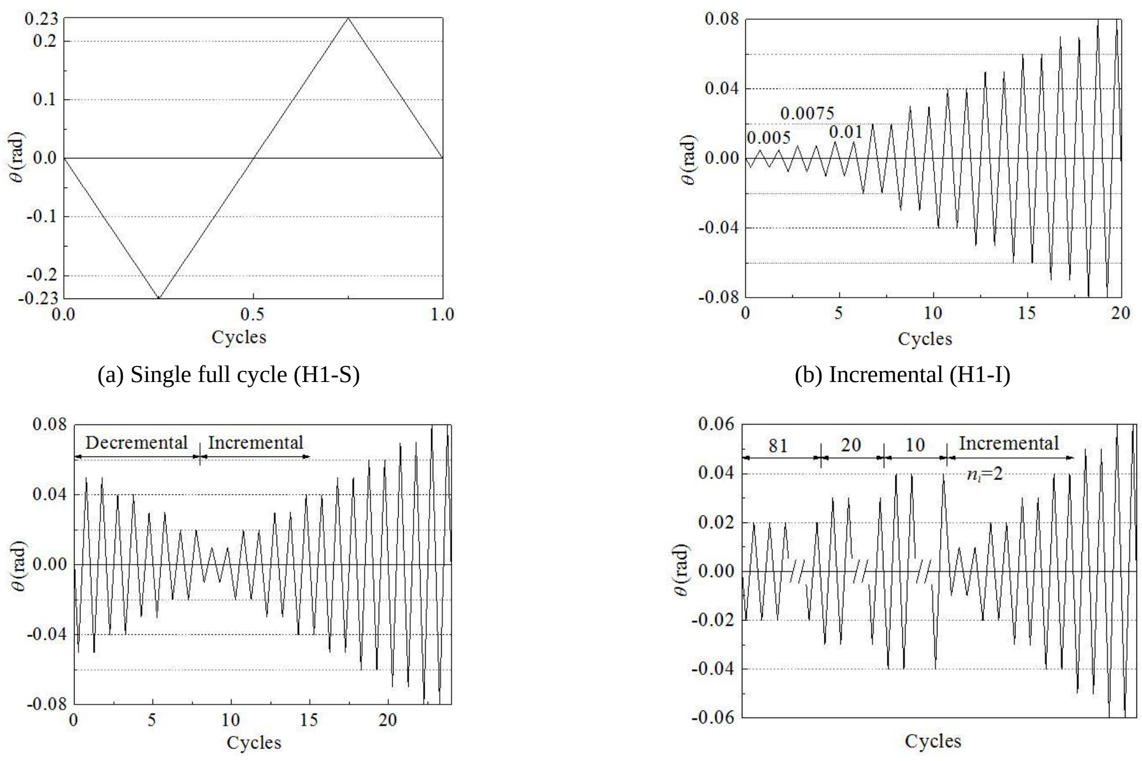

(a) Single full cycle (H1-S)

(b) Incremental (H1-I)

(c) De-incremental (H1-D)

(d) 2-stage incremental (H1-2)

Fig. 3 Loading histories

which is large enough considering the loading histories in this study. Based on the displacement capacity of the actuators, the maximum rotational capacity of the loading beam was ±14°. In addition, the positive and negative loading directions are also illustrated in Fig. 2.

2.3 Loading history

For the experiments, 4 different loading histories were designed to investigate the effect of loading history on seismic performance of the H-shaped steel beams under ULCF loading. The employed 4 loading histories are shown in Fig. 3, including single full cycle loading, incremental loading, de-incremental loading and 2-stage incremental loading. The single full cycle loading history shown in Fig. 3(a) is to simulate pulsed excitation during a strong earthquake, which is close to the case of monotonic loading. For the single full cycle loading, the beam was loaded till the rotational capacity of the loading device and then reversal loading was applied. The incremental loading history is widely employed in cyclic tests, which was thus selected. The de-incremental loading history was employed to investigate the effect of the loading sequence on ULCF properties of the specimen. The 2-stage incremental loading history has 3 different constant-amplitudes loading with relative small amplitudes followed by the incremental loading, which was designed to investigate the effect of the small amplitude loading reversals on the seismic performance of the specimen.

The deformation parameter employed to control the loading amplitude is the beam end rotation angle, θ, which can be calculated by the displacement and load of the actuator. The net specimen end rotation can be obtained by excluding elastic flexural deformation of the loading beam as illustrated in Fig. 4. The end rotation of the specimen, θ, can be obtained through the following equation,

$$\theta = \alpha - \alpha_M = \theta_{Cal} - \alpha_F - \alpha_M \tag{1}$$

where α is the rigid rotation of the loading beam, α_M is the elastic rotation of the loading beam subjected to the pure bending, θ_{Cal} is the measured rotation of the loading beam end, α_F is the rotation of the loading beam end due to elastic deformation of the cantilevered part of the loading beam under the concentrated force, F, shown in Fig. 4.

The incremental loading history is illustrated in Fig. 3(b) with 2 cycles per each amplitude. The incremental loading history is symmetric in amplitudes and is to simulate far-field earthquakes. For seismic design, cumulative plastic deformation capacity of the beam after yielding is more concerned, and only 2 elastic amplitudes were thus designed for the incremental loading history, which is similar to the ATC-24 loading history (Krawinkler 1992). After yielding, the amplitude increment was set as 0.01 till failure of the beam, and the yielding rotation of the beam is around 0.01 rad.

The de-incremental loading history shown in Fig. 3(c) is a combination of a decremental loading history and an incremental one. The elastic loading amplitudes of the aforementioned incremental loading history was replaced by stepwise decreasing amplitudes with an initial rotation angle of 0.05 rad.

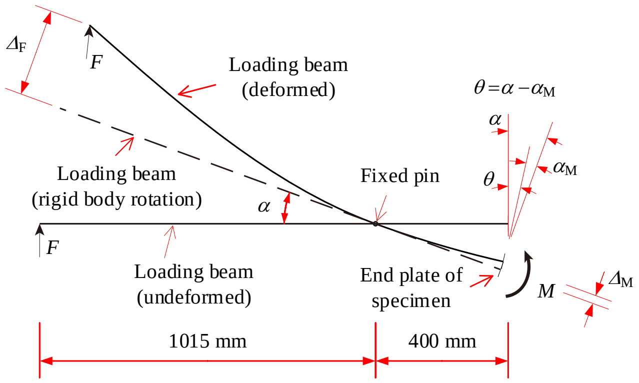

Fig. 4 Calculation of beam end rotation

The 2-stage incremental loading history shown in Fig. 3(d) replaces the elastic amplitudes of incremental loading history with 3 constant amplitudes each with a number of loading reversals. The 3 constant amplitudes were respectively equal to 0.02 rad, 0.03 rad and 0.04 rad, and for each amplitude the number of loading reversals was determined when the absorbed energy under each loading amplitude is equivalent to that under the aforementioned incremental loading history till the peak load. The numbering of the specimens is illustrated by Specimen H1-S, where “H1” denotes Class 1 H-shaped beam, “-S” represents the single full cycle loading history. In addition, “-I”, “-D” and “-2” respectively denotes the incremental, de-incremental and 2-stage loading histories.

3. Experimental results

3.1 Failure modes

The failure processes of the specimens are presented in Fig. 5 and the final states are given in Fig. 6. Fig. 5 indicates that local buckling first occurred at the compressive flange, and then occurred at the compressive web. Under the subsequent loading reversal, local buckling at the other side finally occurred. Strain concentration occurred at the buckled web-to-flange joint, and leaded to ductile crack initiation at the weld toe of the joint. The crack is quite small at the initial stage, and propagated along both the length and thickness directions of the web. Finally, the cracks ran through the web thickness at the location of the weld toes. Fig. 6 indicates that remarkable local buckling deformation occurred at both the beam flanges and the web of each specimen at the final state, and a main crack along the weld toe of the web-to-flange joint ran through the beam web thickness. For Specimen H1-S, no cracking occurred under the first loading reversal which was equivalent to the monotonic loading case, and cracking occurred under the cyclic loading cases due to strain concentration and low ductility of the boundary between the weld and the base metal.

The load-displacement curves shown in Fig. 7 presents the critical states of the specimens and it can be found that the peak loads are all beyond the full-plastic moment of the specimens, indicating that the local buckling is elasto-plastic buckling owing to the small width-to-thickness ratio. The failure process of Specimen H1-S can be divided into the following stages:

(1) The cross-sectional edge stress reached the yield strength of the material, and the corresponding load is denoted as M_y as shown in Fig. 7;
(2) The cross-sectional full-plastic moment was achieved and significant decrease of the tangent modulus of the load-displacement curve shown in Fig. 7(a) can be observed;
(3) Decrease of the material stiffness due to plastic straining finally induced local buckling at the compressive flange when the rotation reached -0.06 rad, while the load still increased owing to the strain hardening effect;

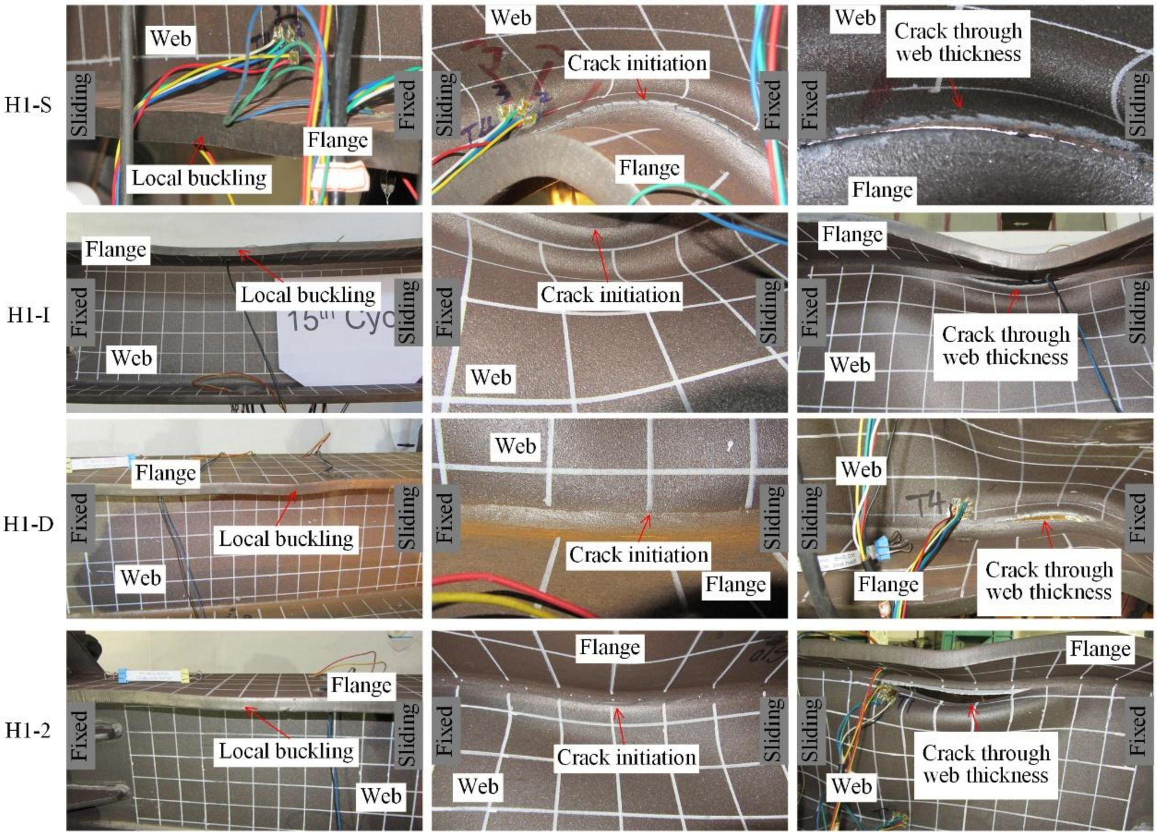

Fig. 5 Failure processes of specimens

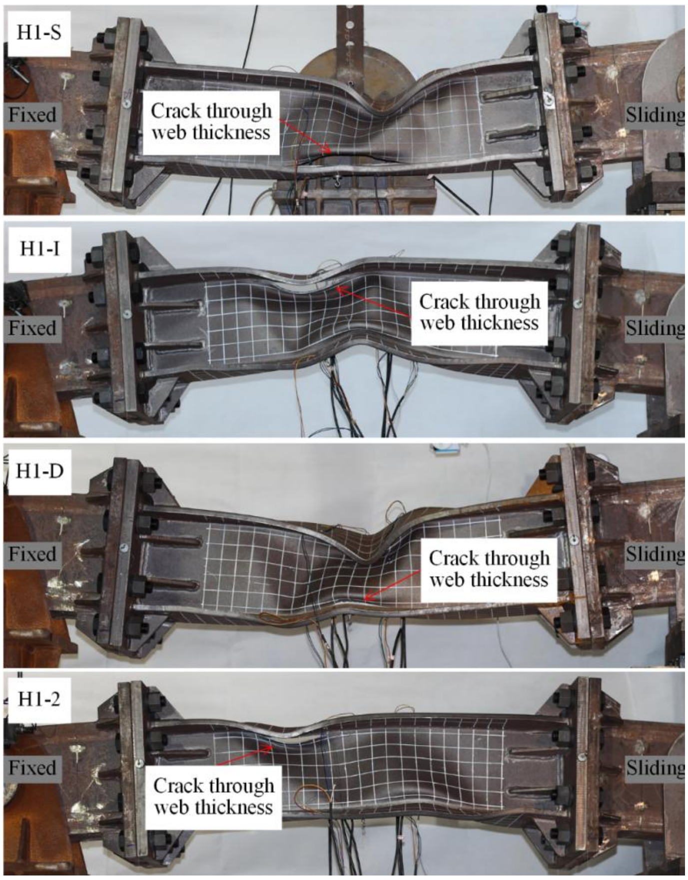

Fig. 6 Final states of specimens

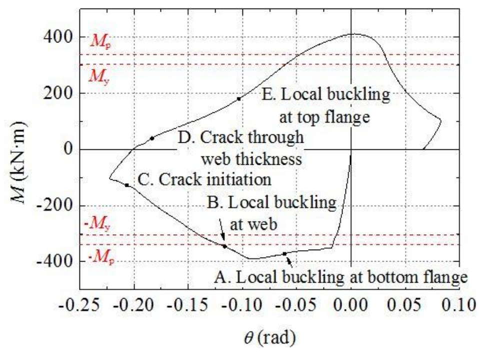

(a) Single full cycle loading

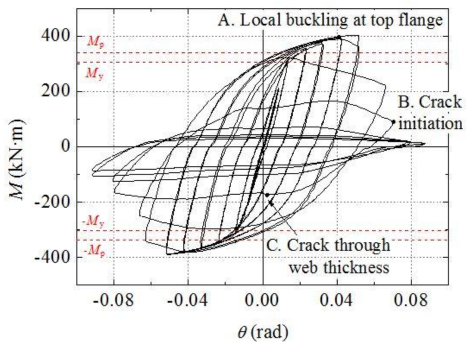

(b) Incremental loading

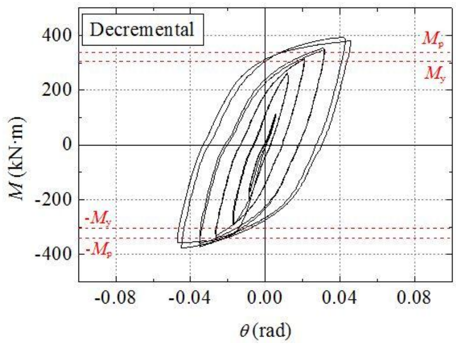

Decremental part

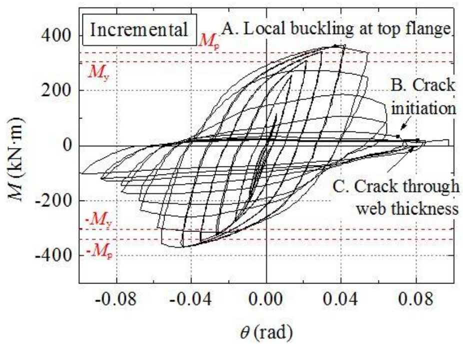

Incremental part

(c) De-incremental loading

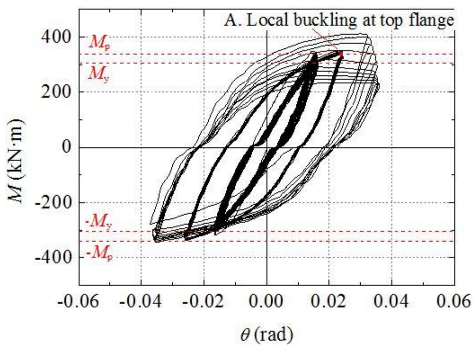

First stage

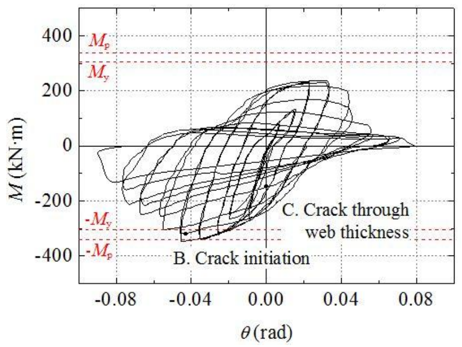

Second stage

(d) 2-stage incremental loading history

Fig. 7 Load-displacement curves of specimens

(4) The load continued increasing till the peak load when the rotation reached -0.09 rad and the load-carrying capacity decreased due to excessive local buckling at the compressive flange;
(5) Local buckling occurred at the compressive web plate when the rotation reached -0.12 rad and the load-carrying capacity continued decreasing;
(6) A crack initiated at the weld toe of the compressive flange-to-web joint as shown in Fig. 5 when the rotation reached -0.21 rad. The cracking was mainly due to strain concentration and relative poor fracture resistance at the boundary between the heat-affected zone and the weld deposit (Liu *et al*. 2017). The crack propagated along the weld length direction, while the crack width was almost unchanged;
(7) The loading direction was reversed and crack propagated quickly along both the weld length and the web thickness directions from the weld toe. The crack finally ran through the web thickness when the rotation reached -0.18 rad;
(8) The crack propagated along the weld length direction, and the cross section at the mid-length of the specimen consisted of the separated bottom flange and a T-shaped cross section as shown in Fig. 6. The load could increase owing to tension of the bottom flange and compression of the T-shaped cross section. Local buckling at the other flange occurred when the rotation reached -0.1 rad;
(9) Loss of load-carrying capacity at the reversal loading half cycle due to excessive local buckling deformation and cracking.

Likewise, the failure process of Specimen H1-I can be divided into the following stages:

(1) The cross-sectional edge stress reached the yield strength of the material and full-plastic moment subsequently;
(2) Local buckling occurred at the first loading cycle of the amplitude of 0.06 rad as shown in Fig. 7(b) and the load continued increasing after the local buckling;
(3) The load-carrying capacity decreased due to excessive local buckling deformation at a rotation of 0.04 rad within the second loading cycle of the amplitude of 0.06 rad;
(4) The load-carrying capacity decreased remarkably due to development of the local buckling deformation at the first loading cycle of the amplitude of 0.07 rad;
(5) A crack initiated at the weld toe of the top flange-to-web joint at the second loading cycle of the amplitude of 0.07 rad, and the load-carrying capacity decreased to 25% of the peak load. This implies that decease of the load-carrying capacity is mainly due to development of local buckling;
(6) The crack propagated along both the weld length and web thickness directions, and ran through the web thickness at the negative half cycle within the second loading cycle of the amplitude of 0.07 rad.

Comparison between the test results of Specimens H1-S and H1-I implies that local buckling both occurred at a rotation of 0.06 rad, while load-carrying capacity of H1-I decreased remarkably at a relative small rotation.

For Specimen H1-D under the de-incremental loading history, the failure process can be divided into the following process:

(1) The cross-sectional edge stress reached the yield strength of the material and full-plastic moment subsequently, and no buckling was found during the decremental loading stage;
(2) Local buckling occurred at the first loading cycle of the amplitude of 0.05 rad during the incremental loading stage as shown in Fig. 7(c), and the load continued increasing after the local buckling;
(3) The load-carrying capacity continued increasing until the first loading cycle of the amplitude of 0.06 rad, and began to decrease as the local buckling deformation became apparent;
(4) A crack initiated at the weld toe of the bottom flange-to-web joint during the incremental loading stage at a rotation of 0.08 rad. At the moment, the load has decreased to 10% of the peak load, indicating minor effect of the cracking on the hysteretic properties under the loading history. As the loading amplitude increased, the crack finally ran through the web thickness.

Comparison of occurrence of the local buckling between Specimen H1-D and those of Specimens H1-S and H1-I indicates that local buckling can happen earlier as the number of plastic loading reversals increases.

For Specimen H1-2, 81, 20 and 10 loading cycles were firstly applied for the amplitudes of 0.02 rad, 0.03 rad and 0.04 rad, respectively. Then incremental loading history similar to that of Specimen H1-I was applied. The failure process is given as follows:

(1) The cross-sectional edge stress reached the yield strength of the material and full-plastic moment subsequently during the loading amplitude of 0.02 rad;
(2) Local buckling occurred at the last loading cycle of the amplitude of 0.03 rad during the constant-amplitude loading stage, and no decrease in the load was observed;
(3) Deterioration of the load-carrying capacity happened from the second loading cycle of the amplitude of 0.04 rad during the constant-amplitude loading stage, and the load continued decreasing as the number of the loading cycles increased. The load has decreased to 56.2% of the peak load at the end of the first loading stage with the 3 constant amplitudes;
(4) Multiple minor cracks initiated at the top weld toe of the flange-to-web joint at the first loading cycle of the amplitude of 0.05 rad, and a main crack ran through the web thickness at the second loading cycle of the amplitude of 0.07 rad.

The test result of Specimen H1-2 shows that occurrence of local buckling is correlated with the loading histories, and excessive plastic straining will lead to a relative small rotation corresponding to occurrence of local buckling. In addition, the specimen can still maintain a substantial load-carrying capacity at the moment of crack initiation. This indicates that fracture is a secondary cause leading to deterioration of the load-carrying capacity of Class 1 H-shaped steel beams under certain ULCF loading histories.

3.2 Hysteretic curves

The hysteretic curves shown in Fig. 7 are plump shuttle-shaped indicating stable and favorable energy dissipation capacity of the specimens. The pinching effect was not observed owing to the fact that the load-carrying capacity could still increase during the post-buckling stage when the local buckling deformation was not small. The skeleton

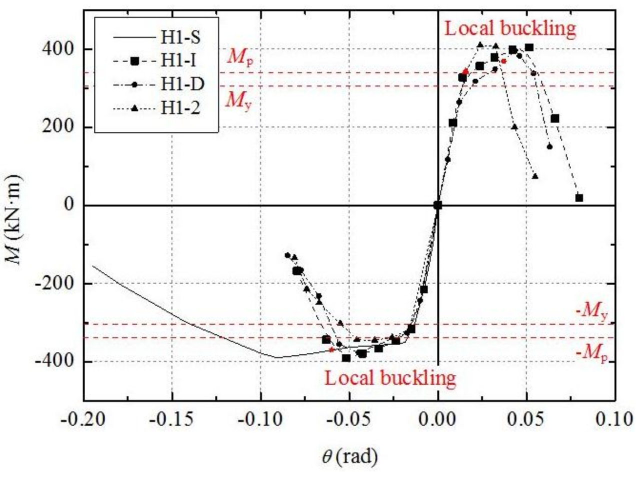

Fig. 8 Skeleton curves of load-displacement curves

Table 3 Experimental results

Specimens	Loading history	Ultimate load (kN.m)	Cumulative plastic ratio	Maximum ductility	Buckling point	Crack initiation point	Loading history	Crack location
H1-S	Single full cycle	390.4	8.3	9.3	0.06 rad	0.21 rad	Single full cycle	Weld toe
H1-I	Incremental	391.5	61.2	8.4	0.06 rad (1st cycle)	0.07 rad (2nd cycle)	Incremental	
H1-D	De-incremental	396.6	91.8	6.9	0.06 rad (1st cycle)	0.08 rad (1st cycle)	De-incremental	
H1-2	2-stage incremental	411.7	200.6	4.1	0.03 rad (20th cycle)	0.05 rad (2nd cycle)	2-stage incremental	

curves of the hysteretic curves are shown in Fig. 8, which indicates that cyclic large plastic straining leads to premature local buckling and also deterioration of the load-carrying capacity. In addition, the initial stiffness and the peak loads of the specimens are close to each other as shown in Fig. 8. The experimental results are also listed in Table 3, where the ultimate loads, buckling and crack initiation points, locations of crack initiation are given.

3.3 Ductility

Ductility indices of a specimen include the maximum ductility, $\mu_{\max}$, and cumulative plastic ratio, μ_c, which can be respectively given by the following equations

$$\mu_{max} = \frac{\theta_{max}}{\theta_y} \tag{2}$$

$$\mu_c = \sum \mu_{pi} = \sum \frac{|\theta_{pi}|}{\theta_y} = \sum \frac{|\theta_i| - \left|\frac{M_i}{K}\right|}{\theta_y} \tag{3}$$

where $\theta_{\max}$ is the maximum rotation, θ_y is the rotation corresponding to yielding of the cross-sectional edge, μ_{pi} is the plastic ratio of the i-th loading half cycle, $|\theta_i|$ is the absolute value of the rotation of the i-th loading half cycle as illustrated in Fig. 9, $|\theta_{pi}|$ is the absolute value of the plastic rotation of the i-th loading half cycle as shown in the figure, M_i is the maximum moment of the i-th loading half cycle, K is initial stiffness of the specimen. The values of $\mu_{\max}$ and μ_c are listed in Table 3, indicating remarkable effect of the loading history on the experimental results. Failure of the specimens was defined when the load decreased to 85% of the peak load, M_u, as illustrated in Fig. 9.

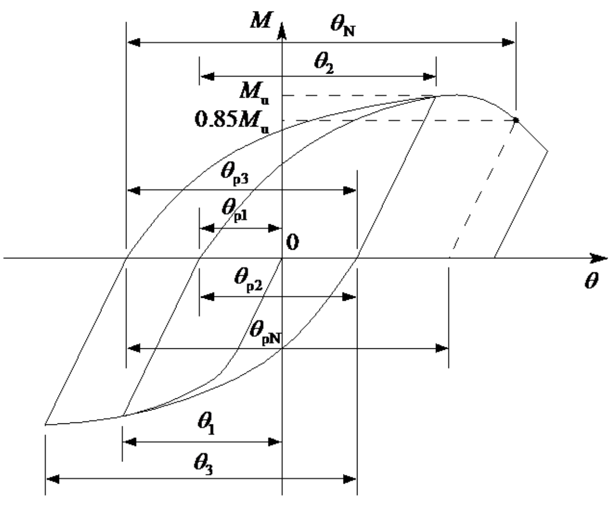

Fig. 9 Illustration of ductility index calculation

According to the Manson-Coffin rule, one can obtain the following equation

$$N_{fi} = C\mu_{pi}^{k} \tag{4}$$

where N_{fi} is the number of loading half cycles under the constant-amplitude loading history with a plastic ratio of μ_{pi}, C and k are constants of the ULCF model.

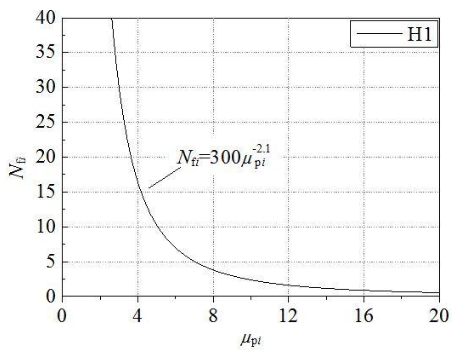

Fig. 10 Failure life prediction

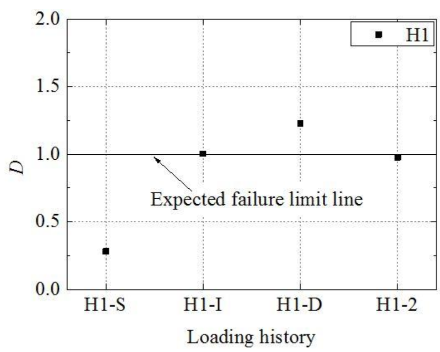

Fig. 11 Damage summation

According to the Miner's rule, one can define an incremental damage index as

$$\Delta D_i = \frac{1}{N_{fi}} \tag{5}$$

where ΔD_i is the incremental damage during the i-th loading half cycle.

$$D = \sum_{i=1}^{N} \Delta D_i = \sum_{i=1}^{N} \frac{1}{C\mu_{pi}^{k}} \tag{6}$$

Failure of the specimen is postulated when D reaches 1.0. Commonly, the values of C and k can be obtained from the experimental results under constant-amplitude loading (Vasdravellis *et al*. 2014). Different amplitudes should be employed to cover the whole strain range that is concerned. In this paper, the values of C and k were calibrated by comparison with the failure points of the experiments under the variable-amplitude loadings due to lack of the test results under constant-amplitude loadings. The fitted C and k are respectively equal to 300 and -2.1. The equation for ULCF life prediction of the Class 1 H-shaped steel beams is plotted in Fig. 10, and the predicted results are also compared with the experimental ones in Fig. 11, indicating that the equation can well evaluate the ULCF of the cyclic loading cases, while great deviation is found for the single full cycle loading case. The first reversal of the single full cycle loading is equivalent to that under monotonic bending. For the single full cycle loading case, i.e., Specimen H1-S, the main difference from the other 3 specimens is its large loading amplitude, which is beyond the amplitude leading to local buckling of the beam under monotonic loading. This leads to an apparent overestimation of the ULCF prediction according to Eq. (6).

4. Ultra-low cycle fatigue life evaluation using an energy approach

In addition to the Manson-Coffin rule, an energy approach can also be employed to evaluate ULCF life of the H-shaped beams. It is known that cyclic hardening of a material can be classified as either isotropic hardening or kinematic hardening. In the literature (Akiyama 1985, Jiao *et al*. 2011), the cumulative energy is divided into 2 types, i.e., isotropic hardening correlated energy and kinematic hardening correlated energy (termed as isotropic energy and kinematic energy in this study for convenience). The total cumulative plastic energy, E_p, is the sum of the 2 energies as shown in Eq. (7).

$$E_p = E_p^i + E_p^k \tag{7}$$

where E_p^i is the isotropic hardening correlated plastic energy, E_p^k is the kinematic hardening correlated plastic energy. However, isotropic hardening in the literature (Akiyama 1985, Jiao *et al*. 2011) was defined to occur when the load was higher than the previous loading reversals. This definition makes the method only applicable to the hardening stage till the peak load. In this paper, new definitions in terms of plastic deformation were given for the isotropic and kinematic energies. The isotropic energy was defined as the one when the absolute plastic deformation was achieved for the first time, and the rest of the cumulative energy was the kinematic energy. The definition method using deformation but not load is more reasonable, since hardening of a material will proceed if only deformation increases. The definition of the isotropic energy is illustrated in Fig. 12, where elastic unloading is postulated. The decomposition method is also illustrated in Fig. 13.

Using the aforementioned method, the isotropic and kinematic energies of the 4 tested specimens non-dimensionalized by the yielding energy can be obtained readily as shown in Fig. 14. It can be found that the kinematic energy takes a large portion of the total dissipated plastic energy. The isotropic energies of the 4 specimens are relative close to each other, and the value decreases with increasing kinematic energy. By regression analysis, a linear relationship between the isotropic and kinematic energies is observed as shown in Fig. 15, which can be described using Eq. (8).

$$\frac{E_p^k}{E_y} = -9.64\frac{E_p^i}{E_y} + 718.7 \tag{8}$$

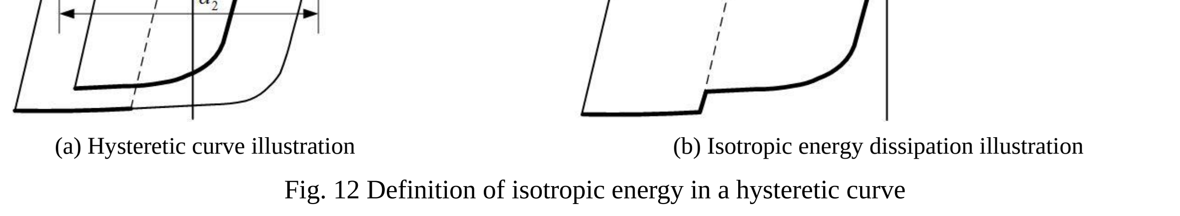

(a) Hysteretic curve illustration (b) Isotropic energy dissipation illustration

Fig. 12 Definition of isotropic energy in a hysteretic curve

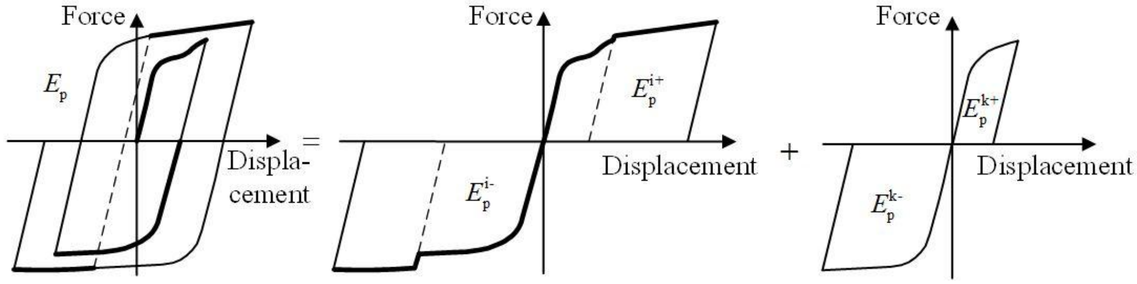

(a) Plastic energy dissipation (b) Isotropic energy dissipation (c) Kinematic energy dissipation

Fig. 13 Decomposition of isotropic and kinematic energies in a hysteretic curve

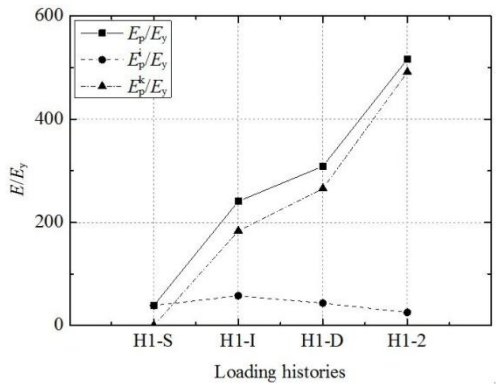

Fig. 14 Dissipated energies of H-shaped beams

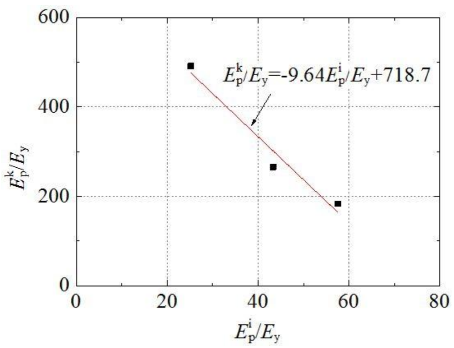

Fig. 15 Correlation between isotropic and kinematic energies for H-shaped beams

where E_y is the elastic energy till yielding of the beam. This formula can be employed to predict ULCF life of Class 1 H-shaped beams under different cyclic loading histories.

5. Numerical simulation

5.1 FE modeling

Finite element models were established in ABAQUS to simulate the experimental results and investigate the capacity of the numerical simulation focused on the evaluation of hysteretic curves and occurrence of local buckling. Three-dimensional models shown in Fig. 16 were established in the implicit analysis module of ABAQUS. The stiffeners, end plates and loading beams were also considered in the numerical models. 4577 linear 4-node shell elements with reduced integration scheme, *S4R*, were employed considering its high efficiency for cyclic large plastic straining problems. Reference nodes were established at the centers of the 4 pin joints of the loading beams, and the pin joints were all simulated through coupling the surrounding nodes with the corresponding reference nodes. The boundary constraints were then directly applied to the reference nodes. The end plates of the specimen were connected with those of the loading beams using the tie elements in ABAQUS. The control scheme was the same as that of the experiments, where displacement data at the loading beam ends were employed.

To simulate the local buckling of the experimental results, initial geometrical imperfection was implemented into the numerical model. Buckling analysis was conducted to obtain the initial imperfection configuration. The initial imperfection consisted of the first 3 buckling modes shown in Fig. 17, and the imperfection configuration Δx can be expressed as

$$\Delta x = \sum_{1}^{3} w_i \cdot \phi_i \tag{9}$$

where w_i = coefficient of the i-th buckling mode; ϕ_i = configuration of the i-th buckling mode. In this study, w_1 = 0.01 t_f, w_2 = 0.005 t_f and w_3 = 0.001 t_f were employed.

5.2 Plasticity model

The combined hardening model in ABAQUS was employed for the numerical analyses. This model is termed as the Chaboche model in this study. The kinematic hardening rule with multiple backstresses is given by the following equation

$$\boldsymbol{\alpha} = \sum_{i}^{n} \boldsymbol{\alpha}_i \,; \qquad \mathrm{d}\boldsymbol{\alpha}_i = \frac{2}{3} C_i \mathrm{d}\boldsymbol{\varepsilon}_\mathrm{p} - \gamma_i \cdot \boldsymbol{\alpha}_i \cdot \mathrm{d}\varepsilon_{eq} \tag{10}$$

where α = total backstress; n = number of backstresses; α_i = i-th backstress; C_i and γ_i = material constants of the i-th backstress; dε_p = plastic strain increment; dε_{eq} = equivalent plastic strain increment. Integration of Eq. (10) under uniaxial stress state gives

$$\boldsymbol{\alpha} = \begin{cases} C_i/\gamma_i \cdot (1\text{-}\mathbf{e}^{-\gamma \varepsilon_{eq}}) & \text{when } \gamma_i \neq 0 \\ C_i \cdot \varepsilon_{eq} & \text{when } \gamma_i = 0 \end{cases} \tag{11}$$

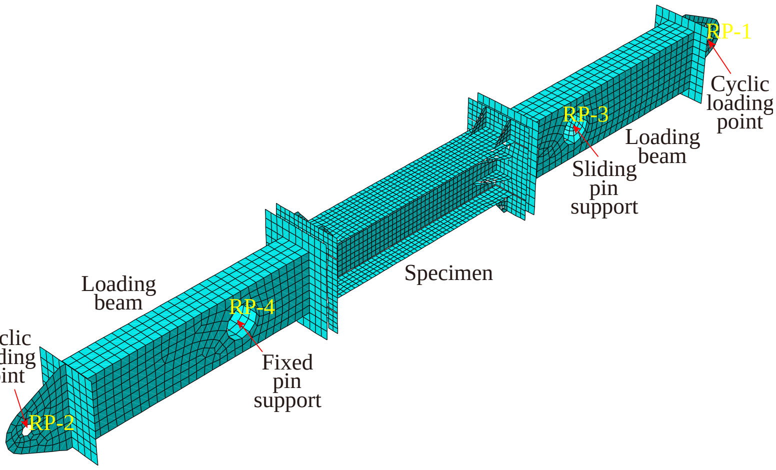

Fig. 16 FE model and mesh

In this study, 3 backstresses were employed with a backtress of linear formation and the other 2 of nonlinear formations. Based on comparison between the experimental and numerical analysis results, the plasticity model parameters were determined as listed in Table 4.

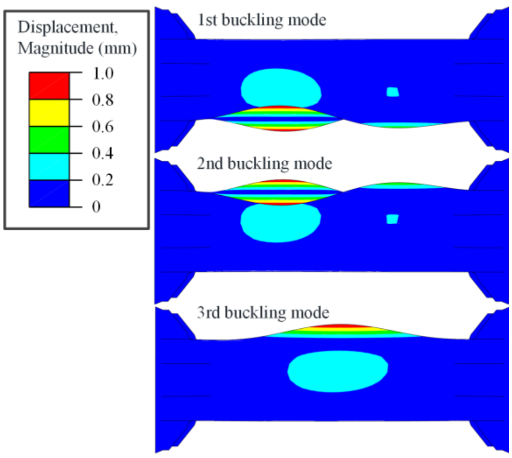

Fig. 17 First 3 buckling modes of beam

5.3 Numerical results

The predicted buckling modes of the specimens are compared with those of the experiments in Fig. 18, and the buckling modes are generally similar to each other. Fig. 18 also indicates that yielding has developed at majority of the cross section for all the specimens at the occurrence of local buckling and only a small region close to the neutral axis is within the elastic state.

Comparison results of the hysteretic curves between the

Table 4 Plasticity model parameters of materials

Location	Yield strength (MPa)	C_1	γ_1	C_2	γ_2	C_3	γ_3
Flange	377	2367	17.3	56	17.4	721	0
Web	428	2735	17.7	251	17.6	721	0

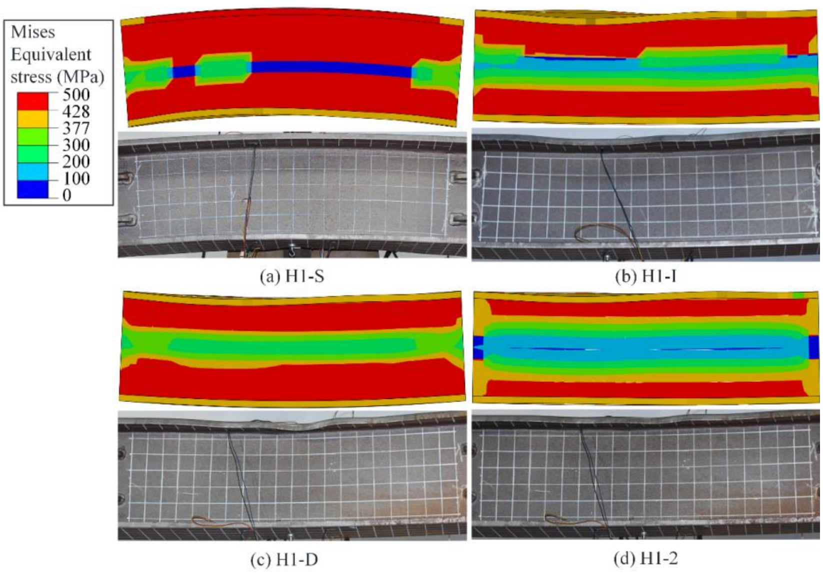

Fig. 18 Comparison of local buckling modes between experimental and numerical results

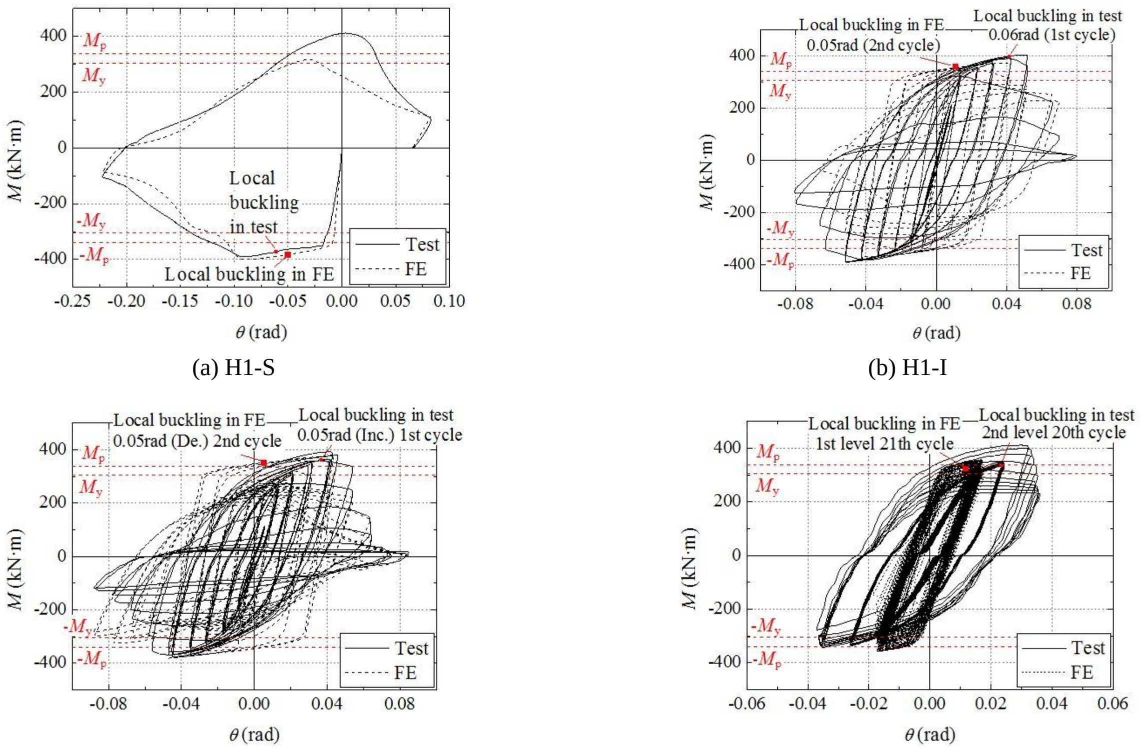

(a) H1-S (b) H1-I

(c) H1-D (d) H1-2

Fig. 19 Comparison of hysteretic curves between experimental and numerical results

experiments and numerical analyses are shown in Fig. 19, implying that the predicted results can compare well for the first 3 specimens while greatly underestimate the ULCF of Specimen H1-2. The underestimation is mainly due to the loss of load-carrying capacity triggered by the premature local buckling as shown in Fig. 19(d). It is known that elasto-plastic buckling is closely correlated with the tangent modulus of the material, which requires accurate prediction of cyclic plasticity of the cross section. The employed Chaboche model gives an overestimation of load at the transition regions as shown in Fig. 19, and the tangent modulus around 0.02 rad was not well evaluated as shown in Fig. 19(d). To solve this limitation, more accurate plasticity models are required to cover the full strain range of the material.

6. Conclusions

In this study, both experimental and numerical studies were conducted for Class 1 H-shaped steel beams under ultra-low cycle fatigue (ULCF) loading. The effects of loading history on failure mode, strength, ductility and cumulative energy dissipation capacities were investigated using 4 different loading histories, i.e., single full cycle loading, incremental loading, de-incremental loading and 2-stage incremental loading as illustrated in Fig. 3. Based on the experimental and numerical results, the following conclusions can be drawn:

- Stable hysteretic curves were obtained for the Class 1 H-shaped steel beams under ULCF loading, and no pinching effect was observed. It was found that the load-carrying capacity could continue increasing even after occurrence of local buckling at the compressive flange owing to the strain hardening effect and the small width-to-thickness ratio.
- Cyclic plasticity can induce decrease in the tangent stiffness of the material and further leads to earlier occurrence of local buckling at the compressive flange. Occurrence of the elasto-plastic local buckling is closely correlated with the plastic straining history, which can be accelerated due to a number of preceding plastic reversals with relative small strain amplitudes.
- Failure of Class 1 H-shaped steel beams under ULCF loading was mainly due to excessive development of the local buckling deformation at both the compressive flange and the web. The load-carrying capacity has decreased below 85% of the peak load when the first crack initiated at the weld toe of the flange-to-web joint for all the specimens. However, a specimen can sustain a substantial load-carrying capacity at the moment of crack initiation under certain ULCF loading history such as the 2-stage loading history in this study. Cracking is the secondary reason leading to strength deterioration of the Class 1 H-shaped steel beams.
- Cracks first initiated at the weld toe of the web-to-flange joint, and propagated along the weld, along with load-carrying capacity decreasing gradually. Finally, the cracks ran through the thickness of the beam web, and all the cracks were ductile.
- The proposed cumulative damage index based on

the Manson-Coffin rule increases nonlinearly as the loading amplitude increases, which can compare well with the experimental results except for the case under a single full cycle loading. Effect of the loading sequence on the cumulative damage was not clearly observed, and this may be correlated with the fact that the elasto-plastic local buckling occurred at a fairly large rotation of 0.06 rad under monotonic loading, and the employed loading amplitudes are all below this value in this study.

- A new energy decomposition method was proposed in this study, where the cumulative energy could be divided into isotropic hardening and kinematic hardening correlated energies. A linear correlation between the 2 energies was observed according to the experimental results, which could be employed to predict ULCF life of the beams.

Acknowledgments

This study is supported by National Key R&D Program of China (2016YFC0701603) and National Natural Science Foundation of China (51178332), which is greatly appreciated.

References

Akiyama, H. (1985), *Earthquake-Resistant Limit-State Design for Buildings*, University of Tokyo Press.

Akrami, V. and Erfani, S. (2015), "Effect of local web buckling on the cyclic behavior of reduced web beam sections (RWBS)", *Steel Compos. Struct., Int. J.*, **8**(3), 641-657.

Anastasiadis, A., Mosoarca, M. and Gioncu, V. (2012), "Prediction of available rotation capacity and ductility of wide-flange beams: Part 2: Applications", *J. Constr. Steel Res.*, **68**(1), 176-191.

Chen, Y., Pan, L. and Jia, L.-J. (2017), "Post-buckling ductile fracture analysis of panel zones in welded steel beam-to-column connections", *J. Constr. Steel Res.*, **132**, 117-129.

Cheng, X., Chen, Y. and Nethercot, D.A. (2013), "Experimental study on H-shaped steel beam-columns with large width-thickness ratios under cyclic bending about weak-axis", *Eng. Struct.*, **49**, 264-274.

Davies, J.M. and Brown, B. (1996), Plastic Design to BS 5950, Wiley-Blackwell.

Dawei, L., Kanao, I. and Nakashima, M. (2003), "Effect of local buckling on plastic rotation capacity of wide flange steel beams subjected to cyclic loading", *Kou kouzou rombunshuu.*, **10**(37), 61-70. [In Japanese]

Elkady, A. and Lignos, D.G. (2015), "Analytical investigation of the cyclic behavior and plastic hinge formation in deep wide-flange steel beam-columns", *Bullet. Earthq. Eng.*, **13**(4), 1097-1118.

Eurocode 3 (2005), Design of steel structures Part 1-1: General rules and rules for buildings, European Committee for Standardization; Brussels, Belgium.

Ge, H.B., Jia, L.-J., Kang, L. and Suzuki, T. (2014), "Experimental study on seismic performance of partial penetration welded steel beam–column connections with different fillet radii", *Steel Compos. Struct., Int. J.*, **17**(6), 851-865.

Gioncu, V. and Petcu, D. (1997a), "Available rotation capacity of wide-flange beams and beam-columns Part 1. Theoretical approaches", *J. Constr. Steel Res.*, **43**(1-3), 161-217.

Gioncu, V. and Petcu, D. (1997b), "Available rotation capacity of wide-flange beams and beam-columns Part 2. Experimental and numerical tests", *J. Constr. Steel Res.*, **43**(1-3), 219-244.

Gioncu, V., Mosoarca, M. and Anastasiadis, A. (2012), "Prediction of available rotation capacity and ductility of wide-flange beams: Part 1: DUCTROT-M computer program", *J. Constr. Steel Res.*, **69**(1), 8-19.

Hall, W.J. (1954), "Shear deflection of wide flange steel beams in the plastic range", Structral Research Series No. 86; University of Illinois Engineering Experiment Station, College of Engineering, University of Illinois at Urbana-Champaign.

Hasegawa, R. and Ikarashi, K. (2014), "Strength and plastic deformation capacity of H-shaped beam-columns", *IABSE Symposium Report*.

Jia, L.-J., Ge, H.B. and Suzuki, T. (2014), "Effect of post weld treatment on cracking behaviors of beam-column connections in steel bridge piers", *Steel Compos. Struct., Int. J.*, **17**(5), 687-704.

Jia, L.-J., Ikai, T., Shinohara, K. and Ge, H.B. (2016), "Ductile crack initiation and propagation of structural steels under cyclic combined shear and normal stress loading", *Constr. Build. Mater.*, **112**, 69-83.

Jiao, Y., Yamada, S., Kishiki, S. and Shimada, Y. (2011), "Evaluation of plastic energy dissipation capacity of steel beams suffering ductile fracture under various loading histories", *Earthq. Eng. Struct. D.*, **40**(14), 1553-1570.

Kasai, K. and Popov, E.P. (1986a), "General behavior of WF steel shear link beams", *J. Struct. Eng. (ASCE)*, **112**(2), 362-382.

Kasai, K. and Popov, E.P. (1986b), "Cyclic web buckling control for shear link beams", *J. Struct. Eng. (ASCE)*, **112**(3), 505-523.

Keisuke, T., Shinji, Y. and Susumu, M. (2006), "Inelastic lateral torsional buckling behavior of H-shaped steel beam-columns", *Summaries of Technical Papers of Annual Meeting Architectural Institute of Japan. C-1, Structures III, Timber Structures Steel Structures Steel Reinforced Concrete Structures*. **2006**, 831-832. [In Japanese]

Ko, O., Toshiro, S., Kikuo, I., Yasuhiro, T. and Hideaki, I. (2000), "Evaluation of plastic deformation capacity of H-shaped steel beam considering the influence of shear stress : Part 1. a property of plastic defomation of H-shaped beam with large width-thickness ratio of web", *Summaries of Technical Papers of Annual Meeting Architectural Institute of Japan. C-1, Structures III, Timber Structures Steel Structures Steel Reinforced Concrete Structures*, **2000**, 487-488. [In Japanese]

Krawinkler, H. (1992), *Guidelines for Cyclic Seismic Testing of Components of Steel Structures*, Applied Technology Council.

Kubiak, T., Kolakowski, Z., Swiniarski, J., Urbaniak, M. and Gliszczynski, A. (2016), "Local buckling and post-buckling of composite channel-section beams–Numerical and experimental investigations", *Compos. Part B-Eng.*, **91**, 176-188.

Lee, G.C. and Lee, E. (1994), "Local buckling of steel sections under cyclic loading", *J. Constr. Steel Res.*, **29**(1-3), 55-70.

Lin, L., Shinji, Y., Susumu, M. and Tatsuya, S. (2002), "Inelastic lateral torsional buckling behavior of H-shaped steel beam-columns subject to double curvature bending moment : Part 3 analysis and discussion", *Summaries of Technical Papers of Annual Meeting Architectural Institute of Japan. C-1, Structures III, Timber Structures Steel Structures Steel Reinforced Concrete Structures*. **2002**, 527-528. [In Japanese]

Lin, L., Yamazaki, S. and Minami, S. (2003), "Experimental study on inelastic lateral torsional buckling of H-shaped steel beam-columns", *J. Struct. Constr. Eng.*, **563**, 177-184. [In Japanese]

Liu, Y., Jia, L.-J., Ge, H.B., Kato, T. and Ikai, T. (2017), "Ductile-fatigue transition fracture mode of welded T-joints under quasi-static cyclic large plastic strain loading", *Eng. Fract. Mech.*, **176**, 38-60.

Nakashima, M. (1994), “Variation of ductility capacity of steel beam-columns”, *J. Struct. Eng.* (*ASCE*), **120**(7), 1941-1960.

Newell, J.D. and Uang, C.-M. (2008), “Cyclic behavior of steel wide-flange columns subjected to large drift”, *J. Struct. Eng.* (ASCE), **134**(8), 1334-1342.

Niu, S., Rasmussen, K.J. and Fan, F. (2014), “Local-global interaction buckling of stainless steel I-beams. II: Numerical study and design”, *J. Struct. Eng., ASCE*, **141**(8), 04014195.

Noritada, I., Shinji, Y., Susumu, M., Lin, L. and Tatsuya, S. (2002), “Inelastic lateral torsional buckling behavior of H-shaped steel beam-columns subjected to double curvature bending moment : Part 1 test results for monotonic loading and cyclic loading”, *Summaries of Technical Papers of Annual Meeting Architectural Institute of Japan. C-1, Structures III, Timber Structures Steel Structures Steel Reinforced Concrete Structures*. **2002**, 523-524. [In Japanese]

Richards, P.W. and Uang, C.-M. (2005), “Effect of flange width-thickness ratio on eccentrically braced frames link cyclic rotation capacity”, *J. Struct. Eng.* (*ASCE*), **131**(10), 1546-1552.

Shinji, Y. (2003), “Analysis of lateral torsional buckling behavior of H-shaped steel beam-columns”, *Summaries of Technical Papers of Annual Meeting Architectural Institute of Japan. C-1, Structures III, Timber Structures Steel Structures Steel Reinforced Concrete Structures*, **2003**, 623-624. [In Japanese]

Shokouhian, M. and Shi, Y. (2014), “Classification of I-section flexural members based on member ductility”, *J. Constr. Steel Res.*, **95**, 198-210.

Shokouhian, M., Shi, Y. and Head, M. (2016), “Interactive buckling failure modes of hybrid steel flexural members”, *Eng. Struct.*, **125**, 153-166.

Vasdravellis, G., Karavasilis, T.L. and Uy, B. (2014), “Design rules, experimental evaluation, and fracture models for high-strength and stainless-steel hourglass shape energy dissipation devices”, *J. Struct. Eng.* (*ASCE*), **140**(11), 04014087.

Xiang, P., Jia, L.-J., Shi, M. and Wu, M. (2017a), “Ultra-low cycle fatigue life of aluminum alloy and its prediction using monotonic tension test results”, *Eng. Fract. Mech.*, **186**, 449-465.

Xiang, P., Jia, L.-J., Ke, K., Chen, Y. and Ge, H.B. (2017b), “Ductile cracking simulation of uncracked high strength steel using an energy approach”, *J. Constr. Steel Res.*, **138**, 117-130.

Yasuhiro, T., Toshiro, S., Kikuo, I. and Hideaki, I. (2000), “Evaluation of plastic deformation capacity of H-shaped steel beam considering the influence of shear stress : Part2. Evaluation of plastic deformation”, *Summaries of Technical Papers of Annual Meeting Architectural Institute of Japan. C-1, Structures III, Timber Structures Steel Structures Steel Reinforced Concrete Structures*. **2002**, 489-490. [In Japanese]

.

BU